AIAA AVIATION Forum
12-16 June 2023, San Diego, CA and Online
AIAA AVIATION 2023 Forum

10.2514/6.2023-3212

Coherence-based Acoustic Source Decomposition of Installed GE F404 Engine Noise[*]

Logan T. Mathews,[†] Kent L. Gee[‡]
Brigham Young University, Provo, Utah, 84602, United States

and
Alan T. Wall[§]
Air Force Research Laboratory, Wright-Patterson AFB, Ohio, 45433, United States

Understanding the acoustic source characteristics of supersonic jets is vital to accurate noise field modeling and jet noise reduction strategies. This paper uses advanced, coherence-based partial field decomposition methods to characterize the acoustic sources in an installed, supersonic GE F404 engine. Partial field decomposition is accomplished using an equivalent source reconstruction via acoustical holography. Bandwidth is extended through the application of an array phase-unwrapping and interpolating scheme. The optimized-location virtual references method is used, and variations on this method are discussed. Apparent source distributions and source-related partial fields are shown as a function of frequency. Local maxima are observed in holography reconstructions at the nozzle lipline, distinct in frequency and space. It is hypothesized that the first local maximum may relate to noise generated by large-scale turbulence structures around and downstream of the supersonic core tip. Other local maxima are correlated primarily with Mach wave radiation originating from throughout the shear layer and into the region downstream of the potential core tip but before the end of the supersonic core. Source-elucidating decompositions show that the order and behavior of the decomposition lends to the local maxima being related to distinct source mechanisms, while between the local maxima, there is a combination of mechanisms active, which is likely the cause of spatiospectral lobes observed previously with other full-scale, supersonic jets.

Nomenclature

AB = afterburner engine condition
CSM = cross-spectral matrix
diag = matrix diagonal
D_j = fully-expanded jet nozzle exit diameter
EWM = equivalent wave model
γ_{ij}^2 = coherence
h = height of jet centerline
$\mathbf{H}_{\mathrm{YP}}$ = transfer matrix
K = number of selected VRs
$\mathbf{L}$ = lower-triangular matrix from Cholesky decomposition
L_c = potential core length
$\tilde{L}_c$ = estimated potential core length
LM = local maximum/maxima
L_s = supersonic core length
$\tilde{L}_s$ = estimated supersonic core length
LSN = noise associated with large-scale turbulence structures
M = number of PFs in sum
MIL = full military power engine condition
MWR = Mach wave radiation
N = number of candidate VR locations

---

[*] Distribution A: Approved for public release; distribution unlimited. Cleared 05/12/2023.
[†] Graduate Student, Department of Physics and Astronomy, AIAA student member
[‡] Professor of Physics, Department of Physics and Astronomy, AIAA Associate Fellow
[§] Research Physicist, Battlespace Acoustics Branch, AIAA member

NAH = near-field acoustical holography
OLVR = optimized-location virtual references
$\mathbf{P}$ = matrix of complex pressures
PCD = partial coherence decomposition
PF = partial field
PFD = partial field decomposition
P_{MUSIC} = MUSIC power
$\mathbf{R}_{\mathrm{noise}}$ = noise subspace matrix
$\boldsymbol{\Sigma}$ = diagonal matrix of singular values
SONAH = statistically optimized near-field acoustical holography
SVD = singular value decomposition
$\mathbf{S}_{\mathbf{xx}}$ = cross-spectral matrix
$\mathbf{u}$ = trial vector
VR = virtual reference
$\mathbf{w}$ = singular vector
$\mathbf{W}$ = matrix of singular vectors
x = distance downstream of jet nozzle axis
$\mathbf{X}$ = VR-selected complex pressures
y = horizontal distance from jet centerline
$\mathbf{Y}$ = NAH-reconstructed complex pressures
z = vertical distance from the ground plane

I. Introduction

NOISE from high-performance military aircraft remains a significant concern for both communities adjacent to military installations and for those who work near the aircraft. Significant progress in the characterization and understanding of supersonic jet noise has been made; however, there remains much to be discovered about these noise sources. Particularly, the observation of multiple-lobed behavior in supersonic jets[1- 9] and a study of lobe properties suggests the existence of several active, quasi-independent acoustic sources in the plume. While hypotheses have been proposed for this phenomenon[3,10,11], none have yet proved conclusive.

Decomposition of acoustic fields can be a powerful tool for characterizing and localizing sources. The ability to isolate independent sources into separable fields can provide significant insight into the location, extent, and behavior of such acoustic sources. While a variety of decomposition methods are available, those of greatest utility separate independent acoustic sources accurately and with physical relevance, providing a basis for the jet noise field in terms of individual source contributions. However, achieving such a decomposition is challenging. If a sound field is created by multiple incoherent sources, the separability of the field is ensured, and the result is obtained straightforwardly. However, given the partial coherence of jet noise, the subsources can be considered neither completely coherent nor incoherent. The existence of multiple sources of noise of finite mutual coherence makes performing a source decomposition difficult. Thus, the development of methods to elucidate such sources is vital for performing physically meaningful results.

One such method, the optimized-location virtual references (OLVR) algorithm, was developed by Wall *et al.*[12] for use in the analysis of supersonic jet noise. This method works in conjunction with near-field acoustical holography (NAH) to provide a physically meaningful partial field decomposition (PFD) based on virtual references (VRs) that are placed near the presumed acoustic source using a NAH reconstruction. Candidate VRs are assigned a likelihood of being near an acoustic source, and VRs are selected to be separated by a coherence criterion, thus increasing the probability of targeting independent (or poorly correlated) sources. The partial field decomposition is then performed using these virtual references as a guide for separating the field.

To achieve meaningful decompositions, however, a mesh of sufficient resolution must be available to separate acoustic fields near the source. For this task, acoustical holography is used to provide a reconstruction of the acoustic field at the nozzle lipline, where the OLVR decomposition can then be performed. In this paper, statistically optimized near-field acoustical holography (SONAH) is employed. This method has been used previously by Wall *et al.*[3] and Leete *et al.*[5], among others, with other full-scale, installed tactical engine analyses.

The purpose of this paper is to investigate source-related characteristics and radiation phenomena of an installed, GE F404 engine using advanced PFD methods. Distinct local maxima are observed in acoustical holography reconstructions near the nozzle lipline. The optimized location virtual references (OLVR) method is used, with some variations on this method being discussed. Multi-lobed radiation behavior in the field is observed at frequencies between local maxima. OLVR decompositions show that, at frequencies where multi-lobed radiation in the field is observed, partial fields containing distinct radiation lobes are present. From this, it is hypothesized that the local maxima likely correspond to distinct source mechanisms such as Mach wave radiation and noise from convecting large-scale turbulence structures and that multi-lobed radiation behavior is likely occurring due to the activity of distinct acoustic source mechanisms in different regions of the flow.

II. Methods

A. Measurement

The Boeing/Saab T-7A Red Hawk is an advanced jet trainer aircraft developed for the United States Air Force and is powered by the F404-GE-103 afterburning turbofan engine. This engine is a further development in the F404 family, which has been the subject of numerous acoustic studies [13-15]. Measurements were made in six runs of five different engine conditions, 75% N2, 82% N2, 88% N2, military power (MIL, maximum non-afterburning power), and maximum afterburner (AB). The analyses in this paper will focus on the average of all six engine runs at MIL and AB, the two highest engine conditions. Variability across engine runs will be discussed further in future work.

Figure 1. Photo of T-7A aircraft measurement with ground-based imaging array highlighted in yellow.

Acoustic data were obtained from an extensive measurement of the T-7A aircraft at Holloman Air Force Base in August 2019. Details of the measurement are given by Leete *et al.*[6] Numerous microphone arrays were deployed to measure the aircraft; however, this study focuses on a 120-element ground array placed near the aircraft, shown in Fig. 1. A schematic of this array is shown in Fig. 2 and is referred to as the imaging array for its primary use in imaging-type analyses such as acoustical holography and beamforming. The array spans a nearly 70 m aperture, from 15 m in front of the exit plane to ~55 m downstream of the nozzle exit. To produce such an aperture with 120 microphones, element spacing was varied based on the expected frequency content. The portion of the array near and ahead of the microphone array reference point (MARP, located at x = 3.96 m) was configured with relatively close microphone spacing, resulting in a higher spatial Nyquist frequency to accommodate broadband shock-associated noise (BSN) and other noise with significant high-frequency content. Notably, elements far downstream were given much greater spacing because of the anticipated dominance of lower frequency Mach wave radiation (MWR) or large-scale structure noise (LSN). This allowed for a greater aperture to be captured with a limited number of microphones, while not sacrificing fidelity in areas where higher frequency content is expected to dominate.

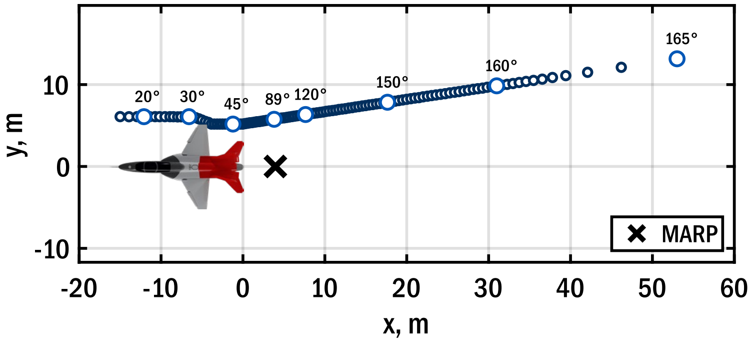

Figure 2. Schematic of the imaging array layout for the T-7A measurement.

B. Bandwidth Extension

Conventional acoustic imaging techniques are bandwidth-limited by the spatial separation of transducers in the measurement. Such limitations ordinarily constrain results to frequencies below the design frequency/spatial Nyquist frequency of the array. Analyses at higher frequencies result in spatial aliasing that compromises the accuracy of the reconstructions. Given the limited number of transducers and large spatial aperture of this measurement, acoustical holography is limited to ~400 Hz and below at the densest portion of the array. However, significant information about the jet noise source is contained above this frequency (such as the dominant energy from BSN). Thus, pursuing methods for bandwidth extension is needed to provide more information about the broadband jet noise source.

One method of extending the bandwidth of array-based measurements is the unwrapped phase array interpolation (UPAINT) method. This method, adapted from Goates *et al.*[16], spatially interpolates the magnitude and phase of the cross-spectral matrices produced by the measurement. Key to this technique is unwrapping the aliased phase between each microphone pair in the cross-spectral matrices. Conventional unwrapping techniques may be used, however, this paper applies a coherence-based pairwise phase unwrapping technique discussed by Cook *et al.*[17] well suited to partially-coherent broadband signals such as those associated with jet noise. With the application of these methods, the results shown in this paper extend far above the array design frequency, up to a frequency of 1 kHz. A brief overview of the UPAINT procedure implemented is given here for reference.

1. Phase Unwrapping

Phase unwrapping is accomplished in a pair-by-pair sense across frequency. A key mistake in phase unwrapping is to unwrap the phase spatially across the array, one frequency at a time (i.e. a 2D phase unwrapping of the cross-spectral matrix at a given frequency). This technique, while it does appear to produce good results (at least when observing the cross-spectral matrix at a given frequency), guarantees no meaningful phase relationship across frequency. Thus, phase unwrapping must be undertaken across the frequency dimension for each microphone pair.

A cross-spectral matrix, $\mathbf{C}$, may be defined from the computed complex pressures along the array as

$$\mathbf{C}(f) = \frac{1}{m}\mathbf{p}_{\boldsymbol{h}}\mathbf{p}_{\boldsymbol{h}}^{\mathrm{H}} = \begin{bmatrix} G_{11}(f) & \cdots & G_{1m}(f) \\ \vdots & \ddots & \vdots \\ G_{m1}(f) & \cdots & G_{mm}(f) \end{bmatrix}$$

Where $\mathbf{p}_{\boldsymbol{h}} = \mathbf{p}_{\boldsymbol{h}}(f)$ is the computed complex pressures along the array, m is the number of measurement points in the array, and $G_{ij}(f)$ is the cross-spectrum between the ith and the jth array element. The magnitude, $|\mathbf{C}(f)|$, and phase $\boldsymbol{\Phi}(f) = \arg\{\mathbf{C}(f)\}$ may be computed directly from the cross-spectral matrix. Phase unwrapping is then accomplished for each given $\Phi_{ij}(f) \in \boldsymbol{\Phi}(f)$. While the methodology for standard phase unwrapping is discussed in Goates *et al.*[16], a coherence-based phase unwrapping technique for $\Phi_{ij}(f)$ is discussed here.

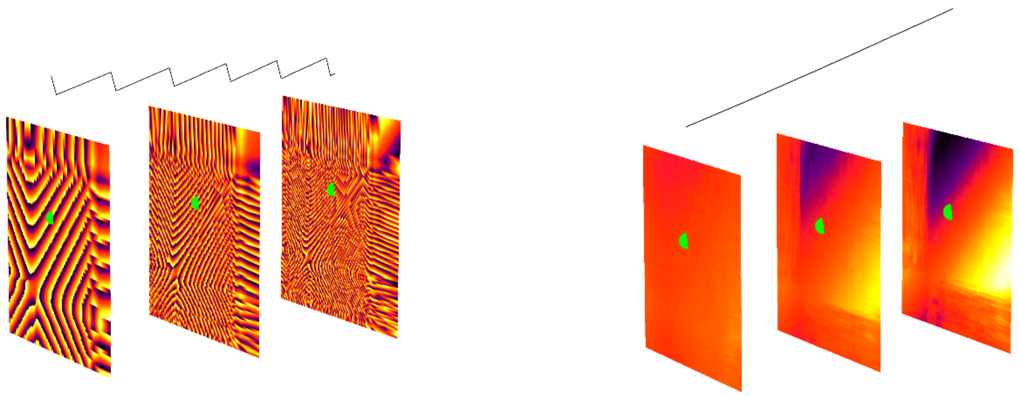

Figure 3. Illustration of phase unwrapping on cross-spectral matrices. Left is shown the unwrapped case, and a sample phase relationship over frequency is shown for a single point on the CSM (indicated by the markers). Right is shown the result after phase unwrapping each microphone pair (and likewise for the same sample point).

Signal coherence becomes an important factor in phase unwrapping when there is poor coherence between the two signals considered. Therefore, coherence is used as a criterion in the unwrapping process to reduce nonphysical phase unwrapping. First, for a given $\Phi_{ij}(f)$, coherence is used to classify which points are of sufficient coherence to allow for phase unwrapping. This is done by selecting some coherence threshold value or scheme to classify points based on their relative coherence. Further discussion on the particular method used here is given by Cook *et al.*[17]. Then, a two-part scheme is used to unwrap the signal. First, those points above the coherence threshold are conventionally unwrapped. Then, a least-squares method is used to unwrap the remaining sub-threshold points based on a selection of the closest neighboring unwrapped super-threshold points. This provides phase unwrapping for the entire signal while reducing the errors introduced by low coherence. An illustrative example of such an unwrapping scheme is shown in Fig. 3, where cross-spectral matrix phases are shown for three distinct frequencies. The phase relationship as a function of frequency for a given pair of microphones ($\Phi_{ij}(f)$) is shown above. The results of unwrapping each pair, $\Phi'_{ij}(f)$, is shown beside. In this case the signals are quite coherent, leading to a linear phase relationship.

C. Acoustical Holography

Statistically optimized near-field acoustical holography is an inverse method developed for a variety of acoustic problems and has been applied to jet noise sources [3,18-20]. An overview of the SONAH process is given here, but more detailed descriptions of the SONAH process may be found in Refs. [21,22], with application to jet-noise-specific problems in Refs. [3,5]. The SONAH process is a method of leveraging a limited measurement array (often referred to as the hologram) to reconstruct acoustic properties at locations of interest. The SONAH process also involves certain techniques to address a limited-aperture measurement of a partially coherent jet noise source.

First, synchronously measured time-domain pressure signals across the array are Fourier transformed to create frequency-dependent cross-spectral matrices (CSMs) that contain both amplitude and phase information. Multiple runups of the engine are used to increase the number of blocks to average over in determining CSMs. Second, the field is decomposed into partial, self-coherent fields using a singular value decomposition (SVD) method. Third, various enhancements are made to mitigate finite aperture and discrete spatial sampling limitations, such as a numerical aperture extension using an analytic continuation method (see Ref. [23]), interpolation, etc. Then, it is assumed that the acoustical behavior at the hologram can be represented as a linear combination of wavefunctions (in a matrix $\mathbf{A}$) that satisfies the linear equation

$$\mathbf{Ac} = \mathbf{p}_{\boldsymbol{h}}, \tag{1}$$

where $\boldsymbol{c}$ is a vector of unknown coefficients and $\mathbf{p}_{\boldsymbol{h}}$ is a vector of measured complex pressures at the hologram. The SONAH algorithm applied in this paper uses an equivalent wave model (EWM) based on a set of cylindrical wave functions defined relative to an axis along the jet centerline. These basis functions, comprised of Hankel functions for the radial component and complex exponentials for the azimuthal and x dependence, are given by

$$\Psi_{l,k_x}(r,\phi,x) \equiv \frac{H_l^{(1)}(k_r r)}{H_l^{(1)}(k_r r_0)} e^{il\phi} e^{ik_x x}, \qquad r \geq r_0, \tag{2}$$

where the radial wavenumber, k_r, is determined by

$$k_r = \begin{cases} \sqrt{k^2 - k_x^2}, & |k| \geq |k_x|, \\ i\sqrt{k_x^2 - k^2}, & |k| < |k_x|, \end{cases} \tag{3}$$

where the second case accommodates evanescent radiation, thus accomplishing the near-field portion of SONAH.

In this paper, only the the $l = 0$ (axisymmetric) case for the set of wavefunctions. Due to the measurement array being confined to the ground, the representation of higher-order azimuthal modes would be inaccurate. In addition, Leete *et al.*[24] showed favorable azimuthal coherence up to several hundred hertz for a high-performance military jet, lending credence to the inclusion of only the axisymmetric wavefunctions for this paper. The complete EWM is then formed as the matrix **A**, given as

$$\mathbf{A} = \begin{bmatrix} \Psi_1(r_{h1}) & \cdots & \Psi_1(r_{hm}) \\ \vdots & \ddots & \vdots \\ \Psi_N(r_{h1}) & \cdots & \Psi_N(r_{hm}) \end{bmatrix}, \tag{4}$$

where *N* is the number of wavefunctions used and m is the number of measurement (hologram) points. Sufficient wavefunctions are generated to construct an effectively complete basis over a source-free region of interest. While no analytical criterion exists for determining what constitutes a complete basis in SONAH, a complete basis is effectively achieved when the addition of additional wavefunctions produces no change in the solution. Additional discussion on the selection of wavefunctions in **A** is given by Hald[22]. In essence, the matrix **A** is a transfer matrix from the hologram to a reference surface very close to the jet centerline. The inverse problem is then formulated as

$$\mathbf{c} = \mathbf{A}^{-1}\mathbf{p}_{\boldsymbol{h}}. \tag{5}$$

In practice, **A** is nonsquare and the inversion is nontrivial. Depending on the dimensions of **A**, the solution is obtained in either a least-squares or minimum-norm sense via a regularized inverse. The realization of either of these solutions results in the statistically optimized portion of SONAH[25]. Regularization filters out high-order wavenumbers associated with non-acoustic measurement noise that would otherwise create significant errors in inward reconstructions. A modified Tikhonov regularization method[26] is employed to accomplish this. Once the inverse problem has been solved, a matrix $\boldsymbol{\alpha}$ is created to propagate out to reconstruction locations:

$$\boldsymbol{\alpha} = \begin{bmatrix} \Psi_1(r_{q1}) & \cdots & \Psi_1(r_{qn}) \\ \vdots & \ddots & \vdots \\ \Psi_N(r_{q1}) & \cdots & \Psi_N(r_{qn}) \end{bmatrix}, \tag{6}$$

where n is the number of reconstruction locations. Like the matrix $\mathbf{A}$, $\boldsymbol{\alpha}$ serves as a transfer matrix from the reference surface out to various reconstruction locations. The inverse problem can then be leveraged to predict acoustic properties at the reconstruction locations by evaluating the linear equation

$$\mathbf{p}_q^{\mathbf{T}} = \mathbf{c}\boldsymbol{\alpha} = \mathbf{p}_h^{\mathbf{T}}\mathbf{R}_{\mathbf{A}^{\mathbf{H}}\mathbf{A}}\mathbf{A}^{\mathbf{H}}\boldsymbol{\alpha}, \tag{7}$$

where $\mathbf{R}_{\mathbf{A}^{\mathbf{H}}\mathbf{A}}$ is the regularized pseudoinverse of $\mathbf{A}^{\mathbf{H}}\mathbf{A}$. Thus, the acoustic behavior at reconstruction locations is obtained from the hologram via a two-step transfer process. The SONAH process shown here is applied to complex acoustic pressure, however, its application can be extended to particle velocity as well, enabling the construction of acoustic intensity[27]. This paper will focus only on the acoustic pressure results.

D. Virtual Reference Decomposition

The OLVR methodology has been previously applied to jet noise measurements by Wall *et al.*[12]. This technique, however, is largely adapted from a PFD technique described by Kim *et al.*[28], who essentially showed that the OLVR method produces physically meaningful partial fields, closely mimicking the expected partial fields in a laboratory experiment.

NAH Reconstruction

To elucidate information about the jet noise source, references should be placed near the jet such that source-related phenomena can be resolved. Kim *et al.*[28] found that the best PFD results were obtained when references were placed as close as possible to the physical sources. However, placing acoustic sensors near the jet is problematic, and thus an acoustic imaging method is employed to project measurements from a more distant location to near the jet, where virtual references can be placed. In this application, SONAH is used to reconstruct the acoustic field at the nozzle lipline, a reasonable proxy for the acoustic source of a jet.

SONAH is an SVD-based NAH method that is used to provide accurate reconstructions of sound fields with multiple sources of limited mutual coherence. The SONAH formulation expresses measured acoustic properties at a microphone array (called the hologram, see Fig. 4a) as a linear combination of appropriately chosen wavefunctions that form a basis for the acoustic field. This poses an inverse problem, where the wavefunction coefficients are determined in a least-squares or minimum-norm sense, producing a best fit of the chosen basis to the measured acoustic field. This set of wavefunctions and optimized coefficients comprises the equivalent wave model (EWM) that can be evaluated at other points of interest and can be thought of as a transfer operator that projects the measurement onto a desired surface or field of interest. This can be summarized as

$$\mathbf{Y}' = \mathbf{H}_{\mathrm{YP}}\mathbf{P},$$

where $\mathbf{P}$ is the measured hologram, $\mathbf{Y}'$ are the reconstructed complex acoustic pressures, and $\mathbf{H}_{\mathrm{YP}}$ is the transfer matrix determined by the SONAH algorithm.

To address multiple sources with limited mutual coherence, SONAH relies on an SVD-based PFD to separate the measured signals into energetically-ordered self-coherent partial fields. This is done before the EWM is determined, thus the EWM is computed for each PF and the resulting field reconstruction is represented as an energetic sum of the resulting partial fields.

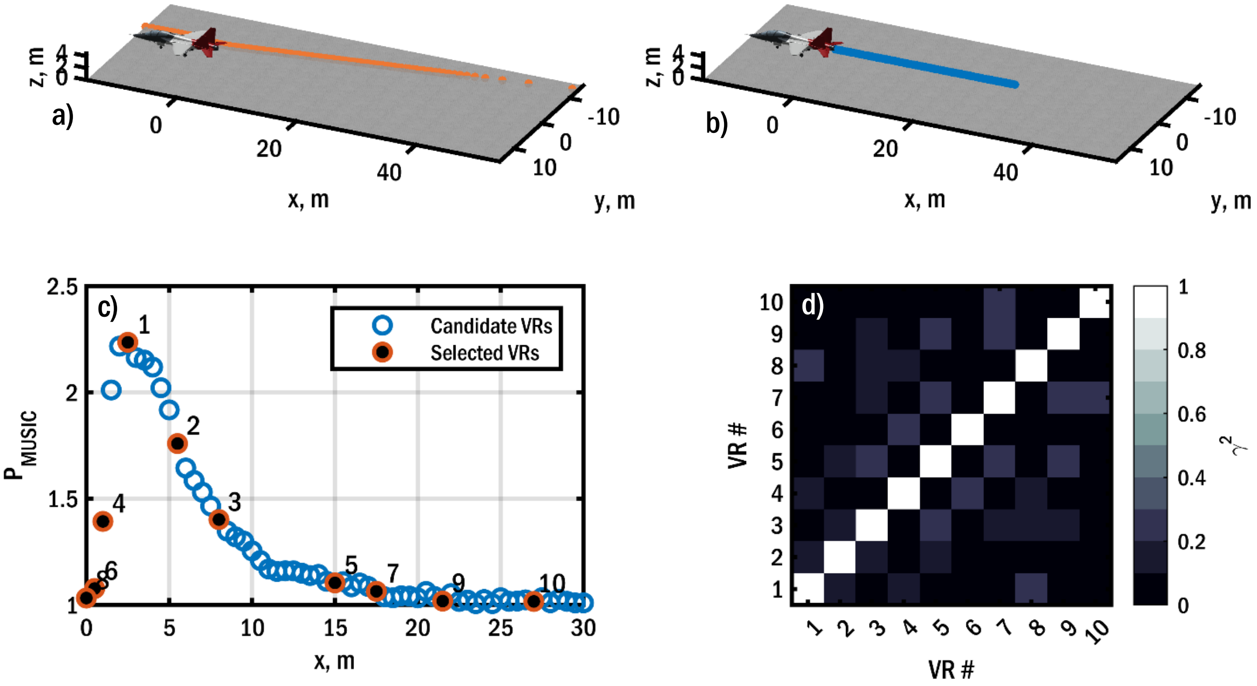

Figure 4. Outline of the virtual reference selection in the OLVR algorithm. (a) Measured hologram, (b) NAH equivalent source reconstruction locations/VR candidate locations along nozzle lipline, (c) MUSIC power at candidate VR locations, with selected VRs shown, and (d) mutual- and self-coherence between selected VRs.

Selection of Virtual References

With an equivalent source representation produced through NAH, virtual references can then be placed in the field that will provide a new basis for separation into physically meaningful partial fields. Notably, virtual references can be placed anywhere in the field with NAH. In this paper, candidate virtual references are placed along the jet lipline (represented in Fig. 4b) to attempt the separation of independent source mechanisms. Candidate VR locations were further spatially restricted to be no farther downstream than the point where the level at the lipline was less than 20 dB from the maximum value. This restriction ensures that candidate locations are placed in regions where meaningful energy is being emitted. The OLVR algorithm uses two subroutines to select virtual references: a metric for determining the likelihood of sources in the vicinity of a virtual reference and a spatial coherence-based separation of virtual references.

To select virtual references that are likely to be near acoustic sources, the multiple signal classification (MUSIC) power[29,30,31] is computed at each candidate virtual reference location. The MUSIC power algorithm provides an estimate of the likelihood an acoustic source is located at any given point. To calculate the MUSIC power, the cross-spectral matrix at each candidate virtual reference location, $\mathbf{S}_{yy}^{N\times N}$, is estimated for every SVD partial field, that is,

$$\mathbf{S}_{yy}^{N\times N} = \mathbf{Y}\mathbf{Y}^{\mathrm{H}}$$

where $\mathbf{Y}^{N\times L}$ is a vector of reconstructed complex pressures at each candidate VR location. Following this, the cross-spectral matrices are decomposed via SVD to obtain

$$\mathbf{S}_{yy}^{N\times N} = \mathbf{W}\boldsymbol{\Sigma}\mathbf{W}^{\mathrm{H}}$$

where $\mathrm{diag}(\boldsymbol{\Sigma}^{N\times N})$ are the singular values and the unitary matrix $\mathbf{W}^{N\times N} = [\mathbf{w}_1\ \mathbf{w}_2\ \cdots \mathbf{w}_N]$ contains the associated singular vectors. If there are $K \le N$ independent sources in the field, then there are K source-related and $N - K$ noise-related singular vectors. Thus, the signal space can be partitioned into two subspaces—one associated with noise and one associated with sources. To construct the noise subspace, $\mathbf{R}_{\mathrm{noise}}^{N\times N}$, we have

$$\mathbf{R}_{\mathrm{noise}}^{N\times N} = \sum_{n=K+1}^{N} \mathbf{w}_n \mathbf{w}_n^{\mathrm{H}}.$$

In practice, determining the order of K for a jet noise source is heuristic. The jet noise source, comprised of turbulence, has no finite number of sources, rather, a quasi-ergodic distribution of turbulent perturbations. Thus, K

must be chosen to represent the total field appropriately. Similar to the approach used by Wall *et al.*[12], K was chosen to be the number of singular values in $\mathbf{\Sigma}$ within 20 dB of $\max(\mathbf{\Sigma})$. This criterion was chosen to be less than the 40 dB in Ref. [12] as the number (and spatial extent) of VRs in this paper are fewer. While this method produces favorable results, further investigation into the estimation of K is warranted.

The noise subspace is then used to determine the MUSIC power at each candidate location. Given the orthogonality of the SVD, $\mathbf{R}_{\text{noise}}$ is orthogonal to the span of the source-related singular vectors. This is exploited in the determination of the MUSIC power. To calculate the MUSIC power, a trial vector is used to "sift" the noise subspace for likely sources. The trial vector is defined as

$$\mathbf{u}_n^{N\times 1} = [0 \cdots 0\ 1\ 0 \cdots 0]^{\mathrm{T}},$$

where the vector is comprised of zeros with only the nth component being unity. The trial vector is, however, alterable based on the type of source, with further discussion given by Kim *et al.*[28]. Further investigation into trial vectors for jet noise sources is needed. The MUSIC power is then calculated for the nth candidate location as

$$P_{\text{MUSIC}} = \frac{1}{\mathbf{u}^{\mathrm{T}}\mathbf{R}_{\mathbf{noise}}\mathbf{u}}.$$

This routine is performed for each of the N candidate VR locations. Due to the orthogonality of the source- and noise-related subspaces, if $\mathbf{u}_n^{N\times 1} = \mathbf{w}_n^{N\times 1}$ for $n = 1$ to K (the source-associated singular vectors), the denominator approaches zero and the MUSIC power becomes infinite. Thus, if the assumed source distribution, $\mathbf{u}_n^{N\times 1}$, matches the "actual" source distribution, the MUSIC power becomes large. Thus, higher values of the MUSIC power calculated with the trial vectors indicate a higher likelihood of being near an acoustic source. In practice, with distributed sources and many candidate VR locations, the range of MUSIC powers calculated is relatively small. The finer the resolution of the virtual reference grid (i.e. the larger the value of N), the smaller the variation in the MUSIC power.

If the field contained ideal point sources, the MUSIC power, computed using this trial vector, would theoretically produce a "comb" like result, that would localize the sources precisely. However, with a distributed source, the MUSIC powers form a smoothly varying distribution, as seen in Fig. 4c. If only high MUSIC powers were chosen without considering the location of these points, the separation of sources would be poor. This is because there are "redundant" virtual references that identify the same source. Kim *et al.*[28] suggests that in the case where the number of incoherent sources is greater than N (i.e. redundancy of candidate VRs is likely), that coherence be used to separate VRs. VRs with high MUSIC power and high mutual coherence likely identify the same source, thus a set of VRs with high MUSIC power and low mutual coherence are sought.

The search for this set of VRs begins by reordering the complex acoustic pressures of all candidate VRs ($\mathbf{Y}^{N\times L}$) in order of MUSIC power as $\mathbf{X}'^{N\times L}$, then calculating the associated cross-spectral matrix $\mathbf{S}_{yy}^{N\times N} = \mathbf{X}'\mathbf{X}'^{\mathrm{H}}$. From this, the coherence between candidate locations i and j is calculated as

$$\gamma_{ij}^2 = \frac{\left|S_{ij}\right|^2}{S_{ii}\,S_{jj}},$$

where S_{ij} is the ijth component of $\mathbf{S}_{yy}^{N\times N}$. Then, an iterative algorithm is used to select the set of VRs with high MUSIC power and low mutual coherence. First, the candidate location with the highest MUSIC power is selected as the first VR. Then, a coherence criterion is chosen, starting with a low value. The second VR is chosen as the location with the next highest MUSIC power whose mutual coherence with the previous VR is less than the coherence criterion. This process is repeated until either K VRs have been identified, or there are no more possible VRs below the coherence threshold. In the latter case, the coherence criterion is then increased, and the process is repeated until a full set of K VRs is found.

Then, a final matrix of coherence-separated, high MUSIC power VRs is constructed as

$$\mathbf{X}^{K\times L} = \begin{bmatrix} \mathbf{Y}_{R_1} \\ \vdots \\ \mathbf{Y}_{R_K} \end{bmatrix},$$

where $\mathbf{Y}_{R_k}$ is the R_kth row of $\mathbf{Y}^{N\times L}$, with R_k being the index of the kth selected VR.

Decomposition by Virtual References

The utility of virtual references is realized in the decomposition technique. With the selected VRs, $\mathbf{X}^{K\times L}$ is decomposed into an orthogonal basis that ideally corresponds to the independent, incoherent sources. The decomposition method used follows the partial coherence decomposition (PCD) method, discussed in detail by Bendat[32]. This method relies upon the Cholesky decomposition to iteratively remove energy from the VR CSM. This CSM is constructed as

$$\mathbf{S}_{\mathbf{xx}}^{K\times K} = \mathbf{X}\mathbf{X}^{\mathrm{H}} = \mathbf{L}\mathbf{L}^{\mathrm{H}},$$

where $\mathbf{L}^{K\times K} = [\mathbf{l}_1\ \mathbf{l}_2\ \cdots \mathbf{l}_K]$ is a lower-triangular matrix of linearly independent vectors, $\mathbf{l}_k$. Due to the nature of the Cholesky decomposition, each vector $\mathbf{l}_k$ contains all energy that is coherent with the kth VR, being removed from $k = 1$ to $k = K$. With this new basis set, the OLVR PFs can then be generated. First, the CSM between all M field points and all K VRs is computed as

$$\mathbf{S}_{\mathbf{xy}}^{K\times M} = \mathbf{X}\mathbf{Y}^{\mathrm{H}}.$$

Then, the OLVR PFs are generated from this CSM using the basis set as

$$\mathbf{P}_{\mathbf{x}}^{M\times K} = \mathbf{S}_{\mathbf{xy}}^{\mathrm{H}}(\mathbf{L}^{\mathrm{H}})^{-1}.$$

This is the final step in the OLVR algorithm. The resulting OLVR PFs, $\mathbf{P}_{\mathbf{x}}^{M\times K}$, are separated based on likely, incoherent sources. This increases the likelihood of PFs being physically meaningful. The OLVR PFs, $\mathbf{P}_{\mathbf{x}}^{M\times K}$, are necessarily ordered spatially according to the VRs as a byproduct of the decomposition method. For this paper, they are finally re-ordered according to integrated energy from highest to lowest.

III. Results

A. Validation

To provide a first-order validation of the holography method, a reconstruction at the imaging array can be compared to the original measurement. Ideally, the reconstructed acoustic behavior should match, but errors are introduced by the holography process. Measured spatiospectral maps along the array are presented in Fig. 5. Noticeable in these maps is the dominant region of radiation which contracts and moves upstream with increasing frequency. Broadband shock-associated noise (BSN) can be observed near the nozzle in each plot at higher frequencies, making a "j" type shape in the maps.

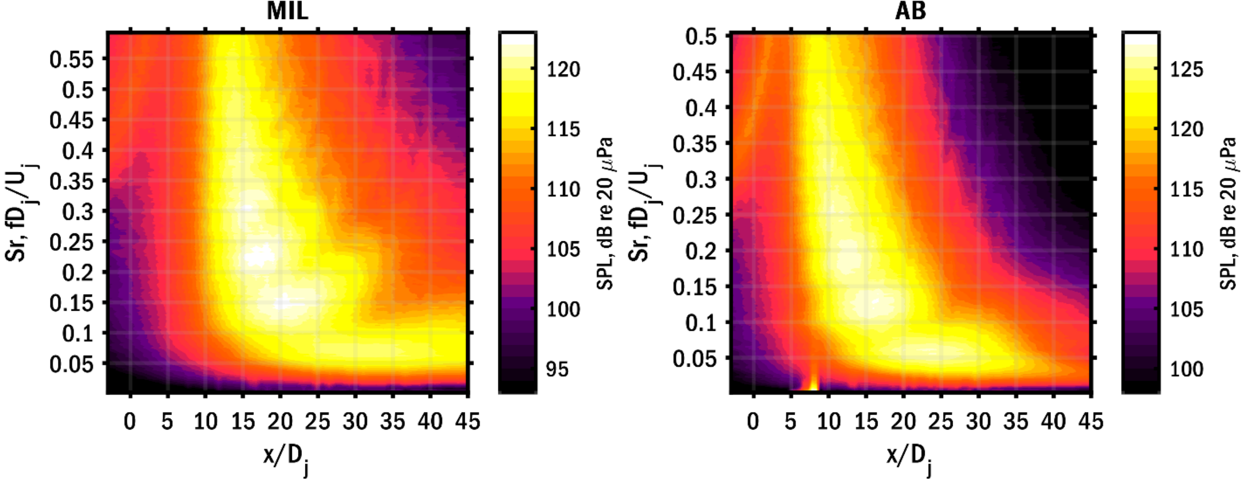

Figure 5. Measured spatiospectral maps along the imaging array for MIL and AB engine conditions.

Figure 6 shows the SONAH reconstruction error at the imaging array for the MIL and AB engine conditions, with and without the application of the UPAINT method. Contours are drawn to show the regions corresponding to the -10 and -20 dB re maximum regions, indicating the areas of greatest energetic importance of the imaging array at each frequency. Although this preliminary application of the UPAINT algorithm introduces errors upstream and downstream of the highest amplitude regions (where the signal is relatively low), it is important to note that it significantly improves reconstruction accuracy within the -10 dB contour. While this first application of UPAINT has yielded appreciable improvements in areas of greatest energy, further refinements are being explored to achieve greater accuracy overall, especially in regions with lower amplitude signals. It is worthy of note that, due to the installed nature of this jet, locations near and upstream of the nozzle/aircraft may have aircraft-related scattering. This may account for some of the difficulty in the phase unwrapping and interpolation near the nozzle seen in Fig. 6, since scattering would likely corrupt or mask the true phase information at affected locations, resulting in erroneous phase unwrapping and/or poor interpolation.

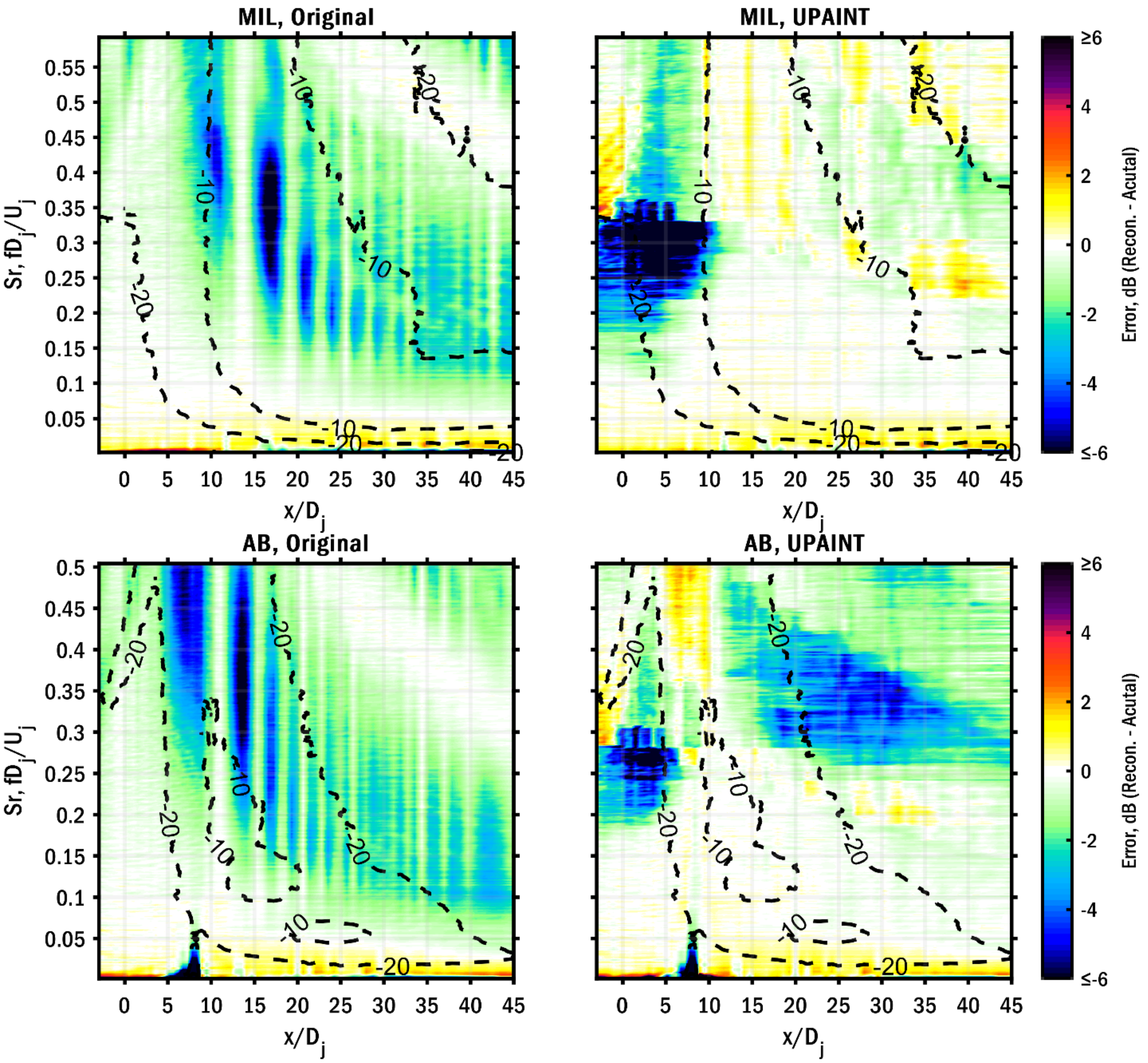

Figure 6. Reconstruction error at the imaging array for MIL and AB engine conditions.

B. Field Reconstructions

Field reconstructions are shown for the ground (z=0) and nozzle centerline heights (z=h) in Fig. 7 for MIL and Fig. 8 for the AB condition at three frequencies of interest, which will be discussed further in subsection C. For both MIL and AB, the higher levels near the nozzle lipline at z=h are apparent, indicative of being near the source. Additionally, for both conditions, the approximate lipline locations of the maximum SPL are roughly the same. Also to note is that the nulls present due to ground reflections in the z=h reconstructions are likely too deep, as has been previously observed with SONAH[33].

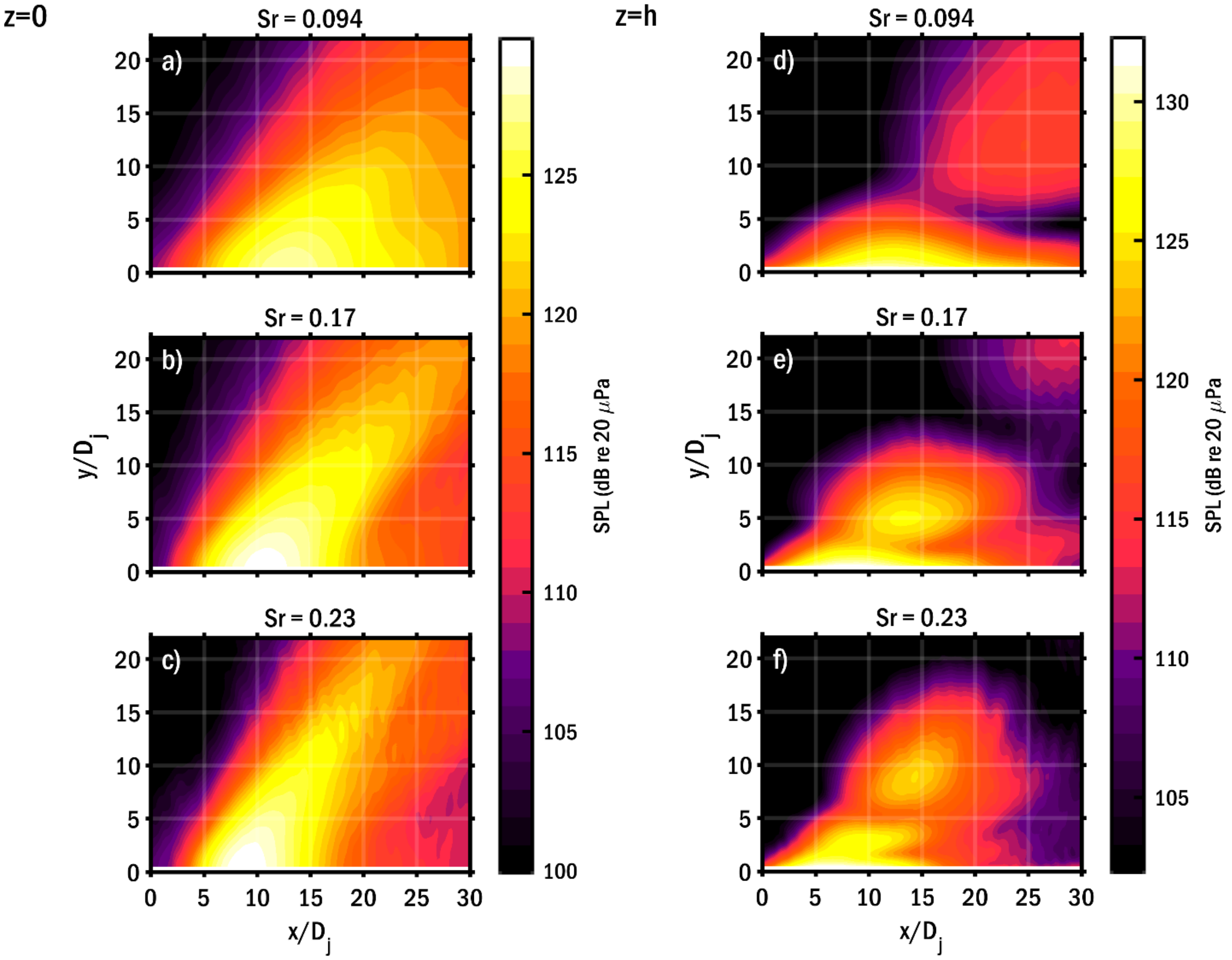

Figure 7. SONAH reconstruction at MIL for three frequencies of interest and at the ground plane ($z = 0$) and the height of the jet centerline ($z = h$).

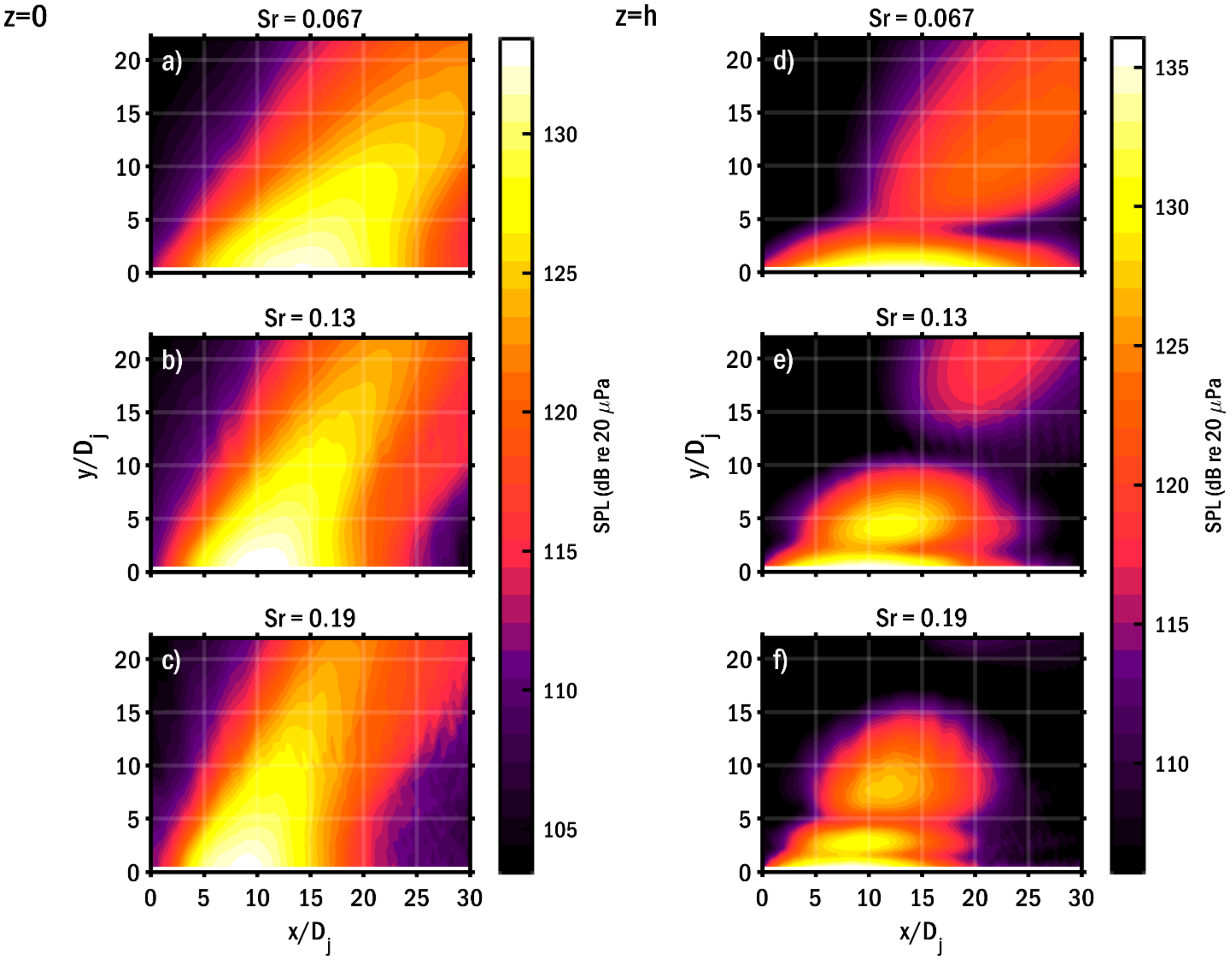

Figure 8. SONAH reconstruction at AB for three frequencies of interest and at the ground plane ($z = 0$) and the height of the jet centerline ($z = h$).

C. Apparent Source Reconstructions and Local Maxima

Spatiospectral reconstructions are performed at the nozzle lipline as an analogous source representation. As the location of actual acoustic sources (turbulent structures under rapid convection) are ill-defined, the nozzle lipline serves as a surrogate for the source region. One could also assume the approximate shear layer, however, for the region considered in this analysis, the difference between the two is very small and the results would be largely equivalent. These spatiospectral source representations are shown in Fig. 9a and c for MIL and AB conditions, respectively. Noticeably, local maxima (LM) are observed, highlighted by contours corresponding to -1 dB re max level in the enclosed region. These LM are similar in appearance to that shown for other tactical aircraft by Leete *et al.*[5] and Wall *et al.*[3], and which have been postulated to be related to the phenomenon of so-called spatiospectral lobes. Local maxima are better defined and occur at lower Strouhal numbers for the AB condition. In these reconstructions, four LM are discernable at MIL with five or more at AB. For this analysis, only the first four LM are considered.

To the right of each of these reconstructions (subplots b and d) are the relative amplitude distributions of the centers of each LM (the centers being indicated by markers in the spatiospectral maps). Overlain on the subplots are the approximate locations of the potential and supersonic core tips ($\tilde{L}_c$ and $\tilde{L}_s$ respectively). More discussion on the approximate location of these regions is given in Mathews *et al.*[34]; see also Leete *et al.*[35] and Liu *et al.*[36,11,37]. Note that the location of L_c and L_s was deduced as reasonable by Mathews *et al.*[34] for the AB condition, however, it is being extended to MIL here. Until high-fidelity simulations can be performed for both the MIL and AB conditions for an F404-type engine, the values for AB will be extended to MIL noting that $\tilde{L}_c$ and $\tilde{L}_s$, are likely to be shorter for MIL than AB, given that evidence points to these regions growing in length with increasing temperature ratio and/or jet velocity, such as is noticed with rockets[38]. Provisionally, a shortening of $\tilde{L}_c$ and $\tilde{L}_s$ of 0.26 and 0.94 diameters has been applied, respectively, for the MIL condition. Further discussion on the rationale behind this adjustment can be found in the appendix.

For both MIL and AB, the energetic order of the LM, from greatest to least, follows the same trend of II, III, I, and IV. Spatially, the LM with the greatest amplitude for both conditions falls between $\tilde{L}_c$ and $\tilde{L}_s$ which has long been regarded as the region of maximum sound power production of the jet. Additionally, for both engine conditions, LM II is the greatest amplitude, with LM III being only slightly lower in amplitude. While LM II is well within the region between $\tilde{L}_c$ and $\tilde{L}_s$, the combination of the two falls very near but just downstream of $\tilde{L}_c$. This is consistent with findings from laboratory-scale heated jets by Baars et al.[39], who observed that the primary flow instability in the jet grew throughout the shear layer, reached a maximum just downstream of L_c, then decayed.

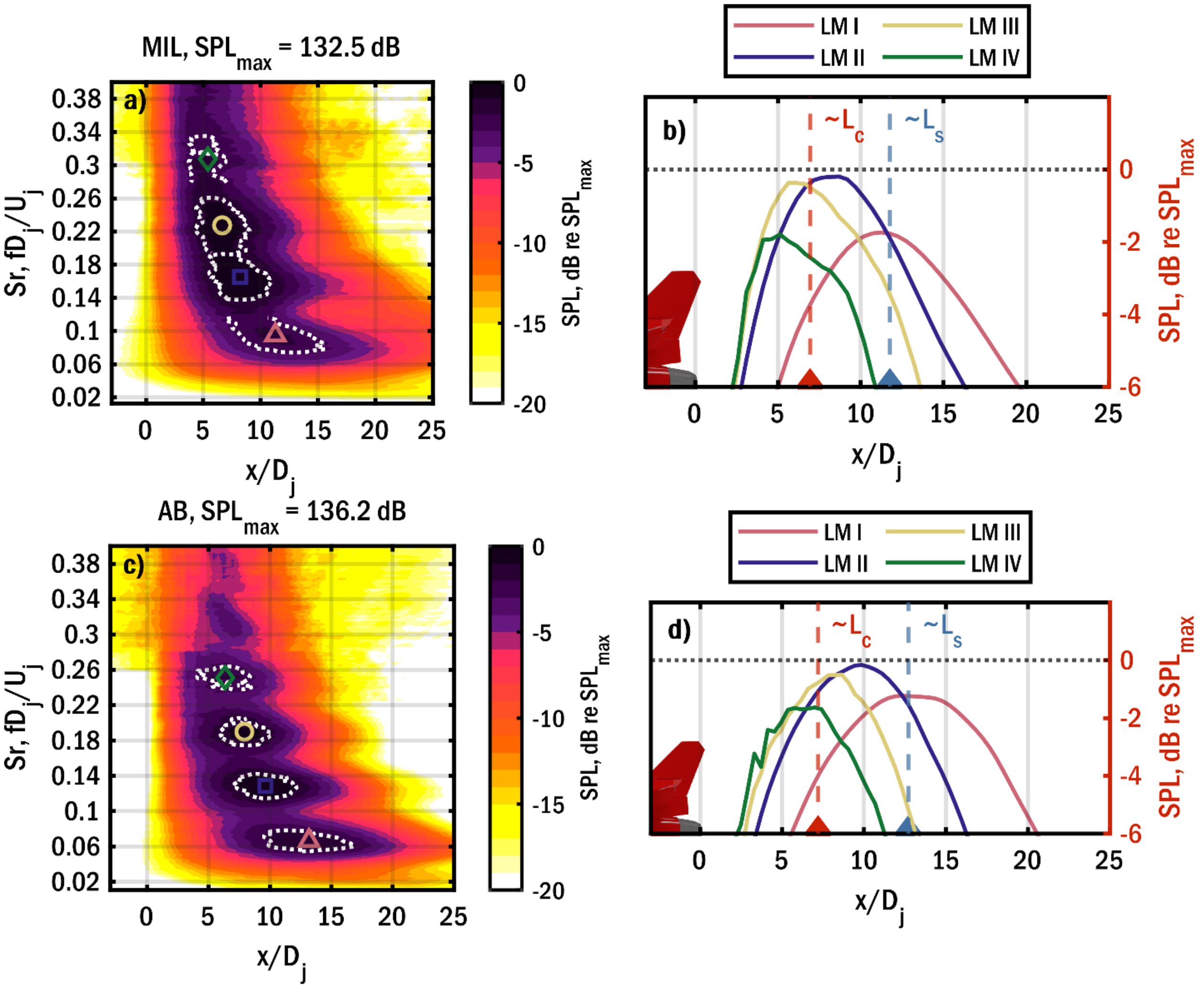

Figure 9. Apparent source spatiospectral reconstructions at the nozzle lipline for MIL and AB conditions. Relative SPL contours are shown for each of the identified local maxima.

D. Source Decompositions

Since the LM indicated in the previous discussion demarcate the most acoustically active frequencies near the source, source decompositions can be performed at these frequencies to describe the spatial distribution of potential acoustic sources that contribute to each of these LM. Additionally, frequencies between these LM are where multiple-lobed behavior is observed in the field, thus decompositions can be performed here to identify separate source phenomena present that contribute to the multi-lobed radiation effect. The OLVR method was used to perform the decompositions at MIL and AB. The coherence criteria used and the number of resulting PFs are summarized in Table 1. Note that with increasing frequency, more OLVR PFs (*N*) were selected in the algorithm, indicating the greater complexity of the field. This has been noticed in the field by Swift *et al.*[40], who showed reduced coherence length with increasing frequency. Appreciably low coherence criteria were also selected, and it is noted that all coherence criteria result in VRs separated by greater than one coherence length. Noticeably, at frequencies between the LM, more OLVR PFs (*K*) were required to represent the source, indicating that there are likely more sources of low mutual coherence at these frequencies. For example, at AB, LM II requires *K* = 7 PFs, and LM III requires *K* = 9. However, between these LM, the number of PFs jumps to *K* = 11. Additionally, the number of OLVR PFs at the lipline within 10 dB of the maximum lipline SPL (*M*) also increased. For example, *M* = 4 for PF II and III, while between them this jumps to six. Similar behavior is present at and between the other LM across both engine conditions shown. If the LM do correspond to distinct, incoherent sources then it would make sense that at frequencies between LM, where principally two LM are contributing to radiation, there would be a greater number of deduced sources of low coherence. In terms of implications for reduced-order models of jet noise, this shows that frequencies around the LM represent relative local minima in terms of the order of models required, while between the LM, higher-order models are required to accurately represent full-scale behavior.

Table 1. OLVR process parameters for each frequency analyzed at MIL and AB engine conditions

Engine Condition	LM#	Sr	γ^2 criterion	*K*	*M*
MIL	I	0.094	0.35	4	3
	I-II	0.13	0.42	6	4
	II	0.17	0.26	5	3
	II-III	0.2	0.37	8	4
	III	0.23	0.12	6	3
AB	I	0.067	0.33	4	3
	I-II	0.097	0.40	8	5
	II	0.13	0.31	7	4
	II-III	0.16	0.40	11	6
	III	0.19	0.32	9	4

Figures 10 and 11 show the results of OLVR decomposition at MIL and AB, respectively. Normalized levels of the first 4 OLVR PFs along the nozzle lipline are shown. Additionally, the relative error is shown between the total reconstructed holography field and the sum of the first *M* OLVR PFs at the ground plane, where *M* has been defined as the number of OLVR PFs within 10 dB of the nozzle lipline maximum value. Contours are drawn on the error plots to demarcate the -10 dB re max region of the field reconstruction. For both MIL and AB, the inclusion of the first *M* OLVR PFs shows highly accurate representations of the acoustic field within the highest amplitude regions with a relatively small number of PFs. Such results show that reduced-order modeling of jet noise can be accomplished with relatively low-order models at these frequencies of interest. In all cases, the greatest error appears in the upstream direction, where the field is known to have low coherence. This has been accommodated previously in reduced-order models by increasing the order (adding more wavepackets)[41], or by the inclusion of a secondary noise source such as a monopole[42].

In examining the OLVR decompositions further, Fig. 10a, corresponding to LM I (Sr = 0.094), consists of one primary OLVR PF, with the other remaining PFs being nearly 10 dB less in peak amplitude. Spatially, this corresponds with the field likely being comprised of one principal acoustic source which appears to be located near $\tilde{L}_s$ as the flow field transitions locally to fully subsonic behavior. For Fig. 10c, corresponding with LM II (Sr = 0.17), there is still one dominant source likely, but with other potential sources being only 7-8 dB lower in amplitude, with one located in the potential core region and another around the $\tilde{L}_s$ and persisting thereafter. Between LM I and LM II in frequency (Fig. 10b), the decomposition yields a primary PF reaching a maximum just after the $\tilde{L}_c$, and a second PF, only about 3 dB less in maximum amplitude, near the end of $\tilde{L}_s$. At this frequency, multi-lobed behavior is observed in total field reconstructions, thus this decomposition suggests that there are two primary active acoustic sources within 3 dB of the maximum magnitude of each other with low mutual coherence (less than or equal to $\gamma^2 = 0.42$). Spatially, these two likely sources appear to have maxima just after the end of $\tilde{L}_c$ and just before the end of $\tilde{L}_s$.

For Fig. 10e, corresponding to LM III (Sr = 0.23), there are similar arrangements of the OLVR PFs as in Fig. 10c, with the dominant field (PF 1) reaching a maximum near $\tilde{L}_c$, with another high-amplitude contributing PF in the potential core region (PF 2). Here, though, the PF in the potential core region is of much higher amplitude, being only 2-3 dB lower in amplitude than PF 1. Thus, it appears that LM III may be comprised primarily of radiation from the shear layer region, with the primary source locations being near or upstream of $\tilde{L}_c$. Finally, at a frequency between LM II and LM III, Fig. 10d shows the PF 1 maximum being just ahead of the $\tilde{L}_c$, with LM III being 2-3 dB lower in amplitude, and the other two PFs being ~7-8 dB lower in amplitude than PF 1.

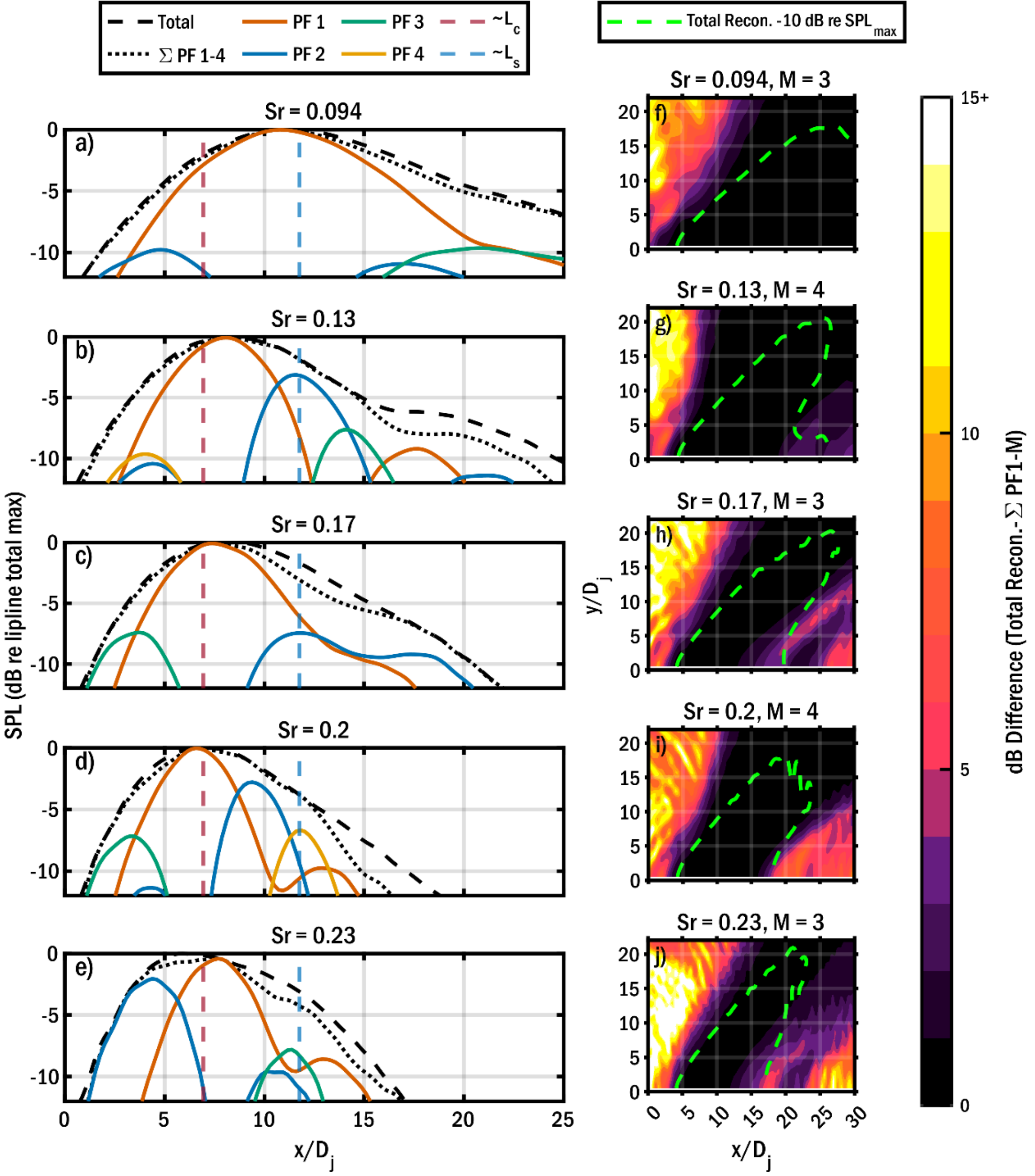

Figure 10. OLVR decompositions for the frequencies corresponding to LM I, II, and III at the MIL condition. Relative partial field levels along the lipline are shown. The relative error at the ground plane is shown between the total reconstruction and the energetic sum of PFs 1-*M*.

For the AB condition, similar trends are observed at MIL, however, PFs of order 2 and beyond are generally higher in amplitude. This is likely related to the reduced coherence lengths present at AB conditions, which has been shown previously by Swift *et al.*[40]. For example, at LM I (Sr = 0.067), there is similar partial source distribution for AB in Fig. 11a as we do for MIL (LM I, Sr = 0.094) in Fig. 10a. However, PF 2 and 3 are on the order of 2-3 dB greater in peak magnitude at AB. This suggests that secondary and tertiary source mechanisms are more active at AB than at MIL.

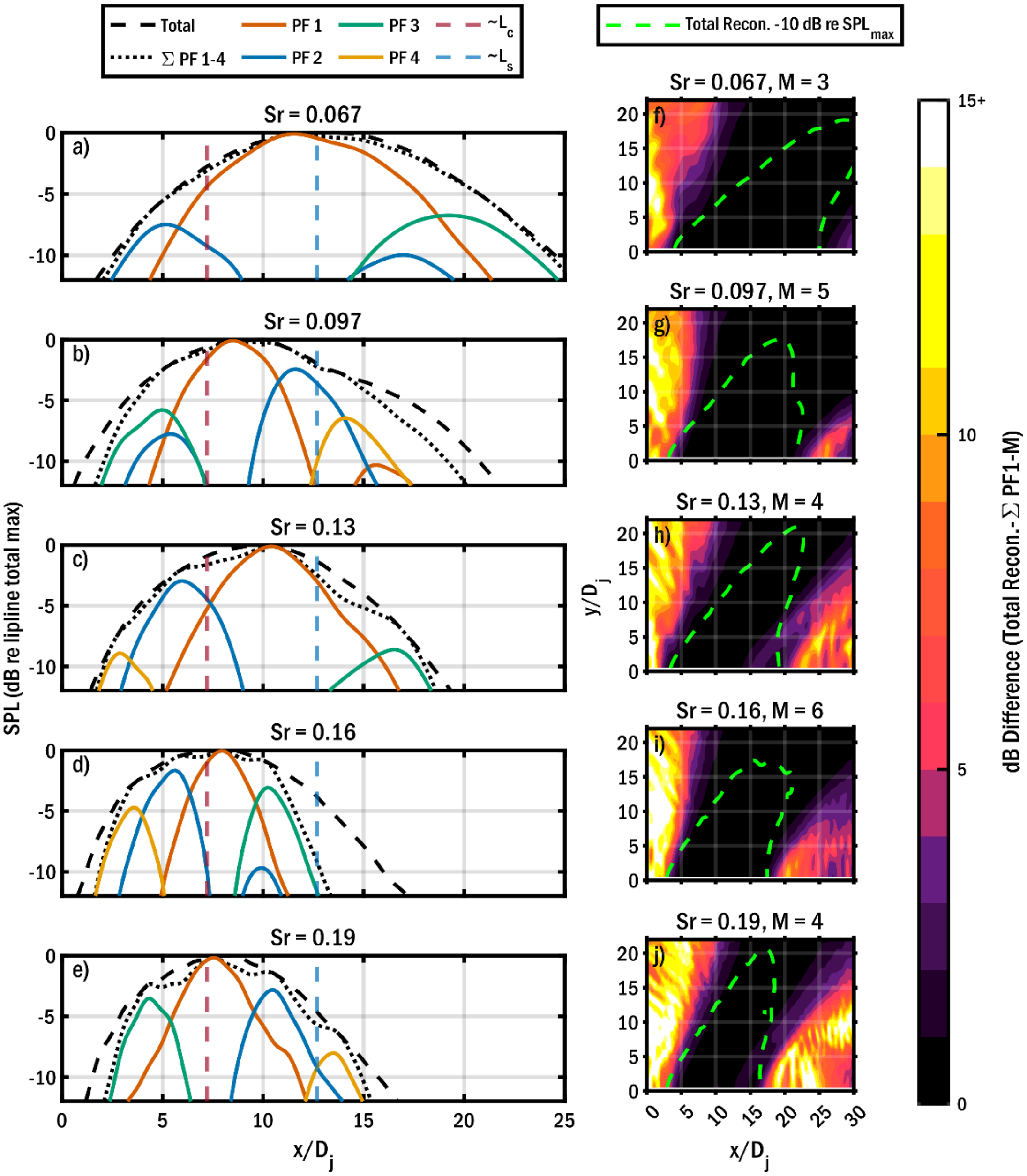

Figure 11. OLVR decompositions for the frequencies corresponding to LM I, II, and III at the AB condition. Relative partial field levels along the lipline are shown. The relative error at the ground plane is shown between the total reconstruction and the energetic sum of PFs 1-*M*.

Figure 12 shows the total field reconstruction and the first four OLVR PFs for each frequency analyzed on the plane z=0 at MIL. Contours are overlain for the -10 dB re max total level. At the frequency corresponding to LM I, PF 1 (Fig. 12b) primarily contributes to the radiation lobe observed in the total field, with PF 2 and PF 3 (Fig. 12c and d) contributing up and downstream of PF 1 at relatively low amplitude. Similar behavior is observed for LM II and LM III. At frequencies between the LM, multiple-lobed radiation behavior is observed in the total field reconstructions (Fig. 12f and p). Between LM II and III in particular, PF 1 primarily contributes to the dominant lobe (Fig. 12q), while PF 2 contributes mainly to the second, less-energetic lobe (Fig. 12r). Note that at both frequencies between LM, the

OLVR PFs are not strictly contributing to one radiation lobe. This is readily observed in Fig. 12g, h, q, and r. While each of these PFs contributes mainly to one lobe, they retain some energy from the other radiation lobe. This aligns with what is understood about spatiospectral lobes; they have low but finite, coherence[40,43,44] thus the presence of some energy of each lobe in a given PF is expected.

Also observable is that each PF at frequencies corresponding to LM has roughly the same directivities, whereas, between the lobes, PFs reflect different directivities. At LM-associated frequencies, the "breaking up" of the single radiation lobe into multiple PFs of similar directivity may be because the source is likely several coherence lengths long. The effect depends on frequency: at Sr = 0.094 (LM I), PF1 (Fig. 12b) contains much of the primary radiation. PF 2 and PF 3 (Fig. 12c-d) are much lower in amplitude. Thus, the splitting of the most energetic source region has a relatively low effect. At Sr = 0.23, however (LM III), PF 1 and PF 2 (Fig. 12v-w) have similar directivities and both have relatively high amplitudes. This may reflect the most energetic region of the source being more than a coherence length long. Harker et al.[45] have shown that coherence length shrinks disproportionately more than the extent of the source region in full-scale supersonic jets, thus, the placement of OLVR VRs less than a coherence length apart results in splitting the primary source region at higher frequencies into multiple PFs. Thus, even though there are multiple high-amplitude PFs at frequencies corresponding to LM, they likely are not attributable to separate source phenomena, as their directivities (and by extension, convective velocities) are similar.

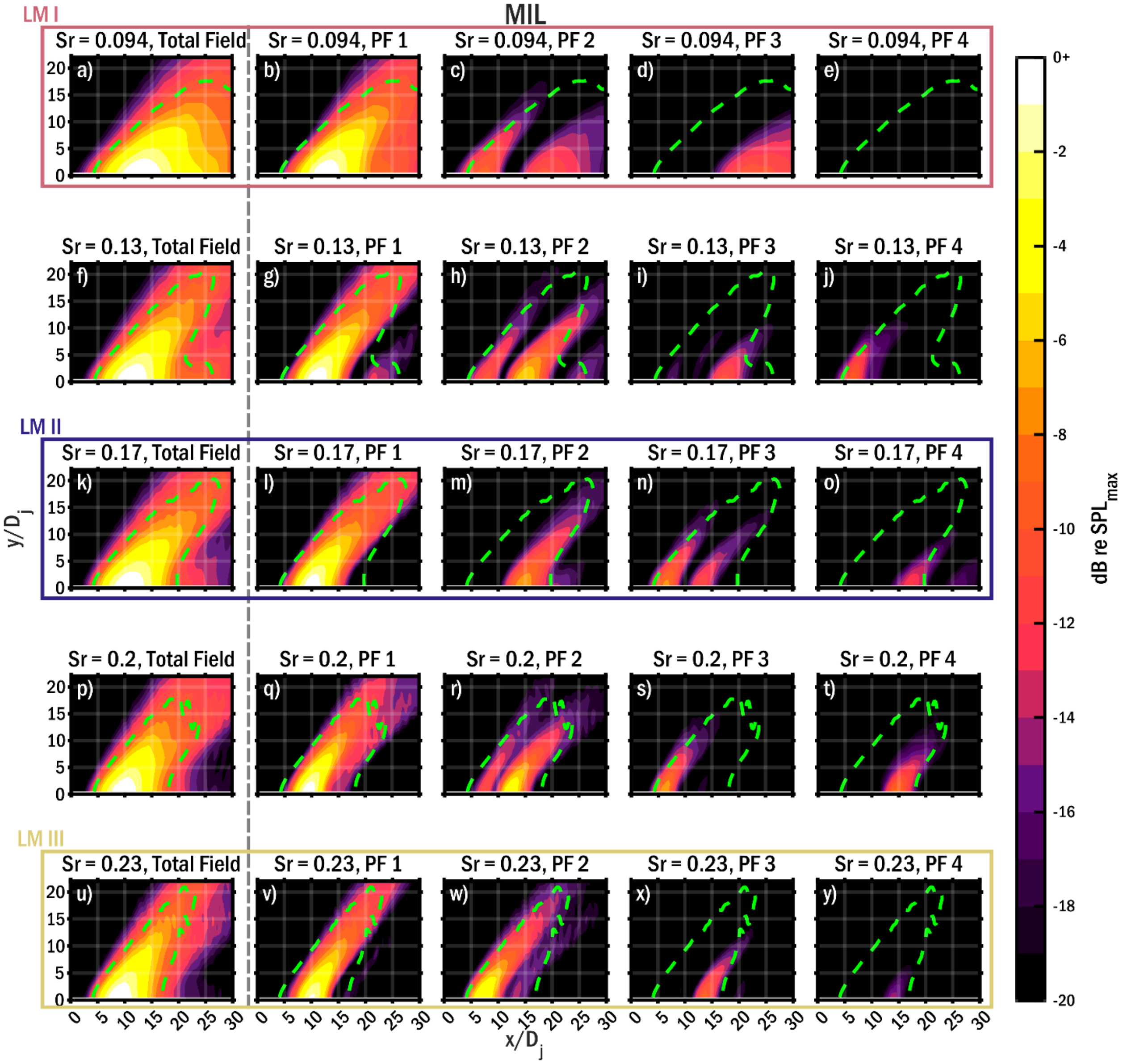

Figure 12. First four OLVR PFs for each frequency analyzed at MIL on the plane z=0. Green dashed contours represent the -10 dB contour on the total field at the frequency of interest. Levels are normalized to the maximum SPL of the total field.

Figure 13 shows the total field reconstruction and the first four OLVR PFs for each frequency analyzed on the plane z=0 at AB. Similar behavior is observed here as at MIL. For the frequency corresponding to LM I, the PFs are highly similar. For both MIL and AB at this frequency, there appears to be one dominant radiation mechanism (shown as PF 1, see Fig. 12b and 13b) that contributes primarily to the main radiation lobe (by about an order of magnitude). This PF has a noticeably more aft-skewed directivity than most of the other frequencies shown. Additionally, PF 1 reaches its maximum level around $\tilde{L}_s$, which is more downstream than the principal PF at any other frequency shown. Given that LSN has been shown to originate farther downstream and have further aft radiation angles[11], it is likely that the dominant noise for LM I at AB and MIL is LSN.

Local maxima II and III have radiation characteristics more in the forward direction, with their most dominant energy coming from upstream of $\tilde{L}_s$. In the case of LM II, the dominant PF has a maximum in between $\tilde{L}_c$ and $\tilde{L}_s$, with the second most energetic PF being just upstream of $\tilde{L}_c$. This could reflect MWR originating from fully-developed turbulence in the region beyond $\tilde{L}_c$ and MWR originating from the shear layer upstream of $\tilde{L}_c$, respectively. While this approach has localized potential sources to these regions and has shown that there are likely distinct acoustic sources in these flow regions, connections to distinct radiation mechanisms are strictly corollary; further work with numerical simulations that connect flow and radiated acoustic energy is necessary to prove causality.

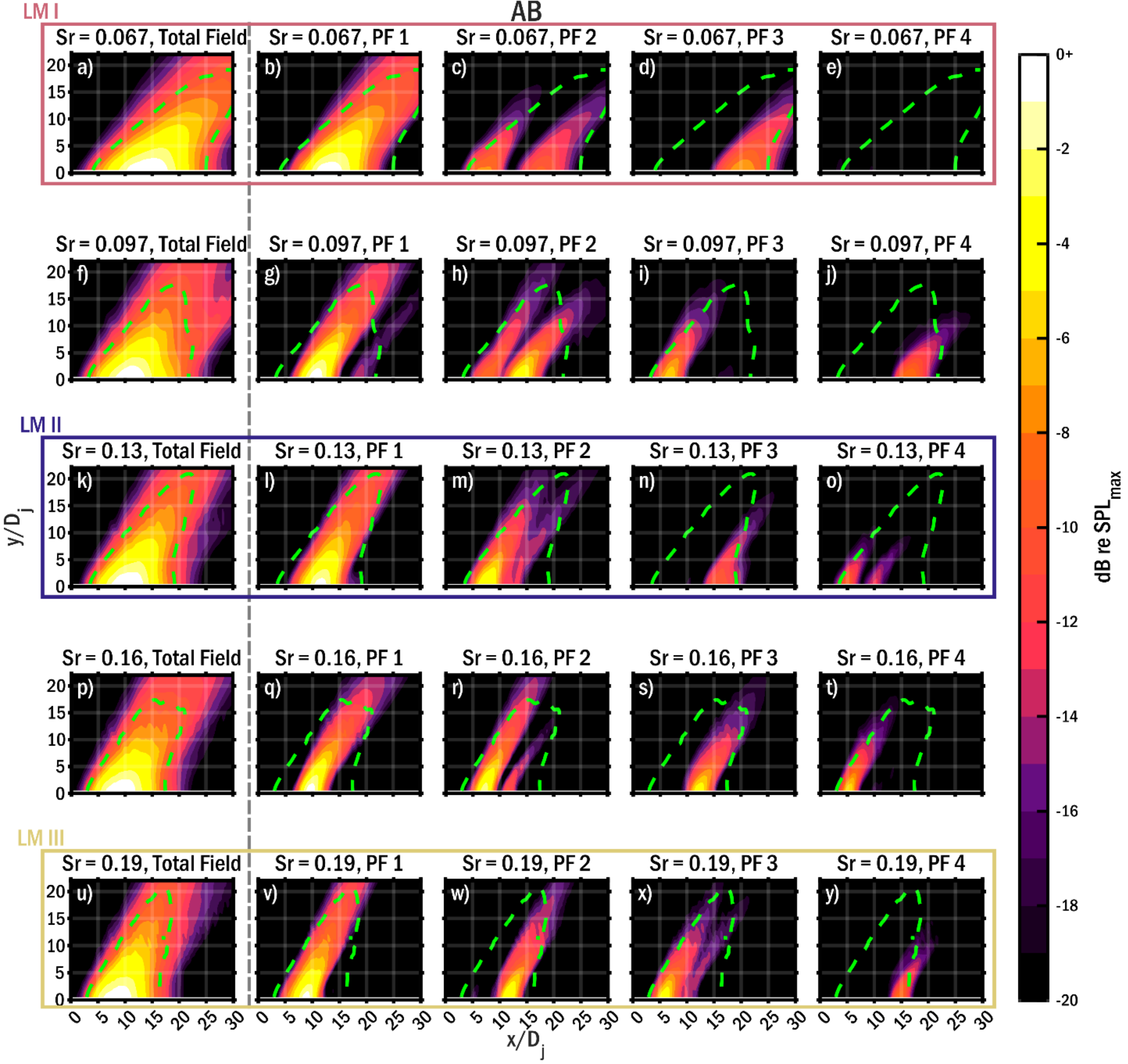

Figure 13. First four OLVR PFs for each frequency analyzed at AB on the plane z=0. Green dashed contours represent the -10 dB contour on the total field at the frequency of interest. Levels are normalized to the maximum SPL of the total field.

Connections can be made between phenomena observed here and in other experiments, both lab-scale and numerical. Schmidt et al.[46] showed, in a characterization of jet flow via LES, that structures throughout the shear layer up to L_c were characterized by Kelvin-Helmholtz-type wavepackets, whereas downstream of the potential core and at lower frequencies, modes associated with Orr-type wavepackets were dominant. The Orr mechanism was found to be present in the shear layer upstream of L_c, but at a much lower amplitude that the Kelvin-Helmholtz mechanism. This identification of mechanisms seems to be consistent with what has been described elsewhere as the mechanisms of MWR and LSN. Liu et al.[11] have shown that in acoustic data from LES that MWR appears to originate from throughout the shear layer and continues downstream some distance. This MWR appears to have broadband behavior. LSN was correlated with an acoustically active region located farther downstream with a lower characteristic frequency. This localization of MWR and LSN seems consistent with observed behaviors of the Kelvin-Helmholtz and Orr mechanisms. Additionally, Liu et al.[11] showed that at AB-like conditions, MWR reached a peak intensity at around Sr = 0.2, while below Sr = 0.1, LSN dominated the radiation. Comparing this with the LM observed in this paper, LM I lies at Sr = 0.067 at AB, while LM II and III are in a region that MWR has been suggested to dominate. This reinforces the idea that LM I may principally correspond to LSN (and by extension, possibly the Orr mechanism), while LM II and III may be primarily attributable to MWR (and therefore, the Kelvin-Helmholtz mechanism in the shear layer and region just after the collapse of the potential core, but before $\tilde{L}_s$).

IV. Conclusion

A coherence-based acoustic source decomposition has been performed at MIL and AB conditions for an installed GE F404 engine using reconstructions obtained via acoustical holography. The application of a phase-unwrapping and interpolation method has been shown to increase the bandwidth of acoustical holography applied to jet noise fields.

These analysis tools have been applied to source characterization efforts. Apparent source representations at the nozzle lipline show local maxima (LM), distinct in space and frequency, at both engine conditions. These local maxima occur further upstream with increasing frequency. Decompositions at and between the frequency centers of the first three local maxima show lower overall numbers of partial fields (PFs) required for representing the field at the LM centers, while between the LM, more PFs are required. Likewise, at frequencies between the LM, more PFs are higher in amplitude than at the LM centers. This suggests lower coherence between the LM centers, and that the field between LM is likely a combination of the phenomena constituting each LM. It seems likely that the first LM may be caused primarily by noise radiation from large-scale turbulence structures, while higher order LM may correspond mainly to Mach wave radiation originating from different regions of the flow- the shear layer and the region just after the collapse of the potential core but before the end of the supersonic core.

While these results are promising, there is considerable research to be undertaken. While analyses of full-scale installed engines such as this are useful for identifying real-world acoustic phenomena, additional tools and analyses are required to directly connect and understand the relationship between flow structure and acoustic radiation phenomena. With such a complex problem of jet noise, proper understanding must be fostered by a combination of full-scale analyses, laboratory-scale experiments, and numerical simulations.

Appendix

While reasonably precise locations of L_c and L_s are not explored here for MIL, estimates can be made for how they would be expected to change from models. Various empirical expressions have been proposed for L_c and L_s, and these can be used to predict the difference between the expected locations of L_c and L_s at MIL and AB using known engine operating parameters. One set of empirical models was published by Nagamatsu *et al.*[47] as

$$L_c = 5.22M_e^{0.9} + 0.22$$

$$L_s = 5M_e^2 + 0.8$$

Note that in the original publication, M_j is used instead of M_e, being referenced as the "jet Mach number", referring to the exit Mach number of the jet. Since the modern convention is to reserve M_j for the fully-expanded jet Mach number, the equations have been adjusted to be congruent with the nomenclature used in this paper.

Another empirical model for L_s comes from Eldred[48], which is stated as

$$L_s = 6.5[1 + (M_e - 1)^2].$$

Commonly used in rocket noise models, Eldred[49] also produced a model for L_c, being defined as

$$L_c = 3.45(1 + 0.38M_e)^2.$$

Feeling that the Eldred model for L_c was too long, Varnier[50] modified the model by a factor of two, while also replacing exit parameters with equivalent fully-expanded parameters resulting in the expression

$$L_c = 1.75\left(1 + 0.38M_j\right)^2.$$

Additionally, Greska *et al.*[51] noted that the data used to produce the Eldred model was primarily in the cold jet regime, thus they produced an empirical model that attempts to include the effects of jet temperature ratio by the inclusion of a convective Mach number first introduced by Oertel[52]:

$$L_c = 3.134\, e^{1.043M_j - M_c}$$

where

$$M_c = \frac{U_j}{c_j + c_a}.$$

Using known jet parameters, the relative change in L_c and L_s from these empirical models for the transition from AB to MIL are given in Table 1. For all models besides the Greska model, L_c becomes shorter at MIL. Curiously, the Greska model predicts a lengthening of L_c at the MIL condition. This is in contrast to what the other models observe about the behavior of L_c. Further investigation is required to understand this particular model and its validity.

Table 2. Estimated changes in L_c and L_s due to changes in operating condition from AB to MIL according to various empirical models

Model	$\Delta L_c = L_{c,\mathrm{AB}} - L_{c,\mathrm{MIL}}$	$\Delta L_s = L_{s,\mathrm{AB}} - L_{s,\mathrm{MIL}}$
Nagamatsu *et al.*[47]	0.26	0.94
Eldred[48]	-	0.46
Eldred[49]	0.25	-
Varnier *et al.*[50]	0.13	-
Greska *et al.*[51]	-0.56	-

Figure 14 shows a comparison plot of each empirical model for core lengths (except for the Greska model), plotted as a function of Mach number (here, M_e and M_j are taken to be equivalent for comparison). Modern core length data from various numerical simulations[35,13,53,39] are also shown. The Nagamatsu *et al.*[47] models for L_c and L_s fits the data reasonably well, with the models by Varnier[50] and Eldred[48] being the least accurate. Thus, ΔL_c and ΔL_s given by the Nagamatsu model are likely the most accurate and for this paper, estimates for L_c and L_s will be reduced by 0.26 and 0.94 diameters, respectively, for the MIL condition.

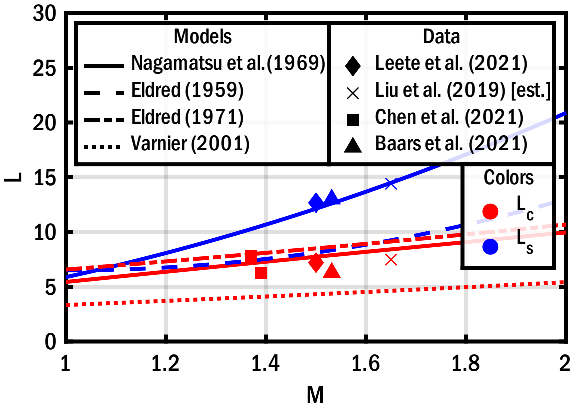

Figure 14. Comparison of empirical core length models and modern experimental data from numerical simulations.

Funding Sources

The authors gratefully acknowledge the Office of Naval Research for funding under grant number N00014-21-1-2069 with project monitor Dr. Steven Martens, Code 351 Jet Noise Reduction. The measurements were funded through the Advanced Pilot Training System Program Office and the Air Force Research Laboratory.

References

[1] Wall, A. T., Gee, K. L., James, M. M., Bradley, K. A., McInerny, S. A., and Neilsen, T. B., "Near-field noise measurements of a high-performance military jet aircraft," *Noise Cont. Engng. J.* **60**(4), 421-434 (2012). doi: 10.3397/1.3701021

[2] James, M. M., Salton, A. R., Downing, J. M., Gee, K. L., Neilsen, T. B., Reichman, B. O., McKinley, R. L., Wall, A. T., and Gallagher, H. L., "Acoustic Emissions from F-35 Aircraft during Ground Run-Up," *AIAA 2015 Aviation Forum*, 22-26 June 2015, Dallas, TX; AIAA 2015-2375. doi: 10.2514/6.2015-2375

[3] Wall, A. T., Gee, K. L., Neilsen, T. B., McKinley, R. L., and James, M. M., "Military jet noise source imaging using multisource statistically optimized near-field acoustical holography," *J. Acoust. Soc. Am.* **139**(4), 1938-1950 (2016).
doi: 10.1121/1.4945719

[4] Tam, C. K. W., Aubert, A. C., Spyropoulos, J. T., Powers, R. W., "On the dominant noise components of tactical aircraft: Laboratory to full scale," *Journal of Sound and Vibration* **422**, 92-111 (2018).
doi: 10.1016/j.jsv.2018.02.023

[5] Leete, K. M., Wall, A. T., Gee, K. L., Neilsen, T. B., James, M. M., and Downing, J. M., "Acoustical Holography-Based Analysis of Spatiospectral Lobes in High-Performance Aircraft Jet Noise," *AIAA J.* **59**(10), 4166-4178 (2021).
doi: 10.2514/1.J059400

[6] Leete, K. M., Vaughn, A. B., Bassett, M. S., Rasband, R. D., Novakovich, D. J., Gee, K. L., Campbell, S. C., Mobley, F. S., and Wall, A. T., "Jet Noise Measurements of an Installed GE F404 Engine," *AIAA SciTech Forum*, 11-15 and 19-21 January 2021, Virtual Event; AIAA 2021-1638.
doi: 10.2514/6.2021-1638

[7] Christian, M. A., Gee, K. L., Streeter, J. B., Mathews, L. T., Wall, A. T., Johnson, J. P., and Campbell, S. C., "Installed F404 Engine Noise Source Characteristics from Far-field Directivity Measurements," *28th AIAA/CEAS Aeroacoustics Conference*, 14-17 June 2022, Southampton, UK, AIAA 2022-3027.
doi: 10.2514/6.2022-3027

[8] Olaveson, T., Ward, J. A., Johnson, J. P., Gee, K. L., Wall, A. T., "Analysis of Spatiospectral Lobes in Installed F404 Engine Noise Radiation," *28th AIAA/CEAS Aeroacoustics Conference*, 14-17 June 2022, Southampton, UK; AIAA 2022-3087.
doi: 10.2514/6.2022-3087

[9] Murray, N. E., Tinney, C. E., and Panickar, P., "Laboratory-Scale Afterburning Supersonic Jet Noise Reduction using Contoured Inserts," *28th AIAA/CEAS Aeroacoustics Conference*, 14-17 June 2022, Southampton, UK; AIAA 2022-3030.
doi: 10.2514/6.2022-3030

[10] Tam, C. K. W., and Parrish, S. A., "Noise of high-performance aircraft at afterburner," *Journal of Sound and Vibration* **352**, 103-128 (2015).
doi: 10.1016/j.jsv.2015.04.010

[11] Liu, J., Corrigan, A. T., Kailasanath, K., and Taylor, B. D., "Impact of the Specific Heat Ratio On the Noise Generation in a High-Temperature Supersonic Jet," in *Proceedings of the 54th AIAA Aerospace Sciences Meeting*, 4-8 January 2016, San Diego, CA; AIAA 2016-2125.
doi: 10.2514/6.2016-2125

[12] Wall, A. T., Gee K. L., Leete, K. M., Nielsen, T. B., Stout, T. A., and James, M. M., "Partial-field decomposition analysis of full-scale supersonic jet noise using optimized-location virtual references," *J. Acoust. Soc. Am.* **144**(3), 1356-1367 (2018).
doi: 10.1121/1.5053580

[13] Liu, J. and Ramamurti, R., "Numerical Study of Supersonic Jet Noise Emanating from an F404 Nozzle at Model Scale," *AIAA SciTech 2019 Forum*, 7-11 January 2019, San Diego, CA, USA; AIAA 2019-0807.
doi: 10.2514/6.2019-0807

[14] Ennix, K. A., Burcham, F. W., and Webb, L. D., "Flight-Determined Engine Exhaust Characteristics of an F404 Engine in an F-18 Airplane," *29th Joint Propulsion Conference and Exhibit*, 20-30 June 1993, Monterey, CA, USA; AIAA 93-2543. See also NASA TM-4538.
doi: 10.2514/6.1993-2543

[15] Seiner, J. M., Ukeiley, L. S., and Jansen, B. J., "Aero-Performance Efficient Noise Reduction for the F404-400 Engine," *11th AIAA/CEAS Aeroacoustics Conference*, 23-25 May 2005, Monterey, CA, USA; AIAA 2005-3048.
doi: 10.2514/6.2005-3048

[16] Goates, C. B., Harker, B. M., Neilsen, T. B., and Gee, K. L., "Extending the bandwidth of an acoustic beamforming array using phase unwrapping and array interpolation," *J. Acoust. Soc. Am*. **141**(4), EL407 (2017).
doi: 10.1121/1.4981235

[17] Cook, M. R., Gee, K. L., Sommerfeldt, S. D., and Neilsen, T. B., "Coherence-based phase unwrapping for broadband acoustic signals," *Proc. Mtgs. Acoust*. **30**, 055005 (2017).
doi: 10.1121/2.0000611

[18] Shah, P. N., Vold, H., and Yang, M., "Reconstruction of Far-Field Noise Using Multireference Acoustical Holography Measurements of High-Speed Jets," *17th AIAA/CEAS Aeroacoustics Conference (32nd AIAA Aeroacoustics Conference)*, 5-8 June 2011, Portland, OR; AIAA 2011-2772.
doi: 10.2514/6.2011-2772

[19] Lee, M. and Bolton, J. S., "Source characterization of a subsonic jet by using near-field acoustical holography," *J. Acoust. Soc. Am.* **121**(2), 967-977 (2007).
doi: 10.1121/1.2404626

[20] Long, D., Peters, J., and Anderson, M., "Evaluating Turbofan Exhaust Noise and Source Characteristics from Near Field Measurements," *15th AIAA/CEAS Aeroacoustics Conference (30th AIAA Aeroacoustics Conference),* 11- 13 May 2009, Miami, FL; AIAA 2009-3214.
doi: 10.2514/6.2009-3214

[21] Wall, A. T., Gee, K. L., and Neilsen, T. B., "Multisource statistically optimized near-field acoustical holography," *J. Acoust. Soc. Am.* **137**(2), 963-975 (2015).

doi: 10.1121/1.4906585

[22] Hald, J., "Basic theory and properties of statistically optimized near-field acoustical holography," *J. Acoust. Soc. Am.* **125**(4), 2105-2120 (2009).
doi: 10.1121/1.3079773

[23] Williams, E. G., "Continuation of acoustic near-fields," *J. Acoust. Soc. Am.* **113**(13), 1273-1281 (2003).
doi: 10.1121/1.1528173

[24] Leete, K. M., Wall, A. T., Gee, K. L., Neilsen, T. B., Harker, B. M., and James, M. M., "Azimuthal coherence of the sound field in the vicinity of a high performance military aircraft," *Proc. Mtgs. Acoust.* **29**(1), 045007 (2016).
doi: 10.1121/2.0000673

[25] Steiner, R. and Hald, J., "Near-Field Acoustical Holography without the Errors and Limitations Caused by the Use of Spatial DFT," *International Journal of Acoustics and Vibration* **6**(2), 83–89 (2001).
doi: 10.20855/ijav.2001.6.278

[26] Williams, E. G., "Regularization methods for near-field acoustical holography," *J. Acoust. Soc. Am.* **110**(4), 1976-1988 (2001).
doi: 10.1121/1.1404381

[27] Stout, T. A., Wall, A. T., Gee, K. L., and Neilsen, T. B., "Obtaining acoustic intensity from multisource statistically optimized near-field acoustical holography," *Proc. Mtgs. Acoust.* **33**(1), 055002 (2018).
doi: 10.1121/2.0000835

[28] Kim, Y. J., Bolton, J. S., and Kwon, H. S., "Partial sound field decomposition in multireference near-field acoustical holography by using optimally located virtual references," *J. Acoust. Soc. Am.* **115**(4), 1641-1652 (2004).
doi: 10.1121/1.1642627

[29] Schmidt, R. O., "A Signal Subspace Approach to Multiple Emitter Location and Spectral Estimation," Ph.D. Dissertation, Stanford University, November 1981.

[30] Schmidt, R. O., "Multiple Emitter Location and Signal Parameter Estimation," *RADC Spectrum Estimation Workshop*, October 1979, Griffiss Air Force Base, NY. Reproduced as: Schmidt, R. O., "Multiple Emitter Location and Signal Parameter Estimation," *IEEE Trans. Antennas Propagat.* **34**(3), 276-280 (1986).
doi: 10.1109/TAP.1986.1143830

[31] Johnson, D. H., and Dudgeon, D. E., "Array Signal Processing: Concepts and Techniques," Prentice-Hall, Englewood Cliffs, NJ (1993).

[32] Bendat, J. S., "Modern analysis procedures for multiple input/output problems," *J. Acoust. Soc. Am.* **68**, 498-503 (1980).
doi: 10.1121/1.384760

[33] Ward, J. A., Gee, K. L., Olaveson, T., and Wall, A. T., "Comparing holography and beamforming inverse methods applied to jet noise radiation near a high-performance military aircraft," *Proc. Mtgs. Acoust.* **35**, 040007 (2022).
doi: 10.1121/2.0001620

[34] Mathews, L. T., Gee, K. L., Leete, K. M., and Wall, A. T., "Acoustic Source Characterization of an Installed GE F404 Engine Using Near-field Acoustical Holography," *28th AIAA/CEAS Aeroacoustics Conference*, 14-17 June 2022, Southampton, UK; AIAA 2022-3028.
doi: 10.2514/6.2022-3028

[35] Leete, K. M., Gee, K. L., Liu, J., and Wall, A. T., "Coherence Analysis of the Noise from a Simulated Highly Heated Laboratory-Scale Jet," *AIAA J.* **58**(8), 3426-3435 (2020).
doi: 10.2514/1.J059112

[36] Liu, J., Corrigan, A. T., Kailasanath, K., and Gutmark, E. J. "Impact of Chevrons on Noise Source Characteristics In Imperfectly Expanded Jet Flows," *21st AIAA/CEAS Aeroacoustics Conference*, 22-26 June 2015, Dallas, TX; AIAA 2015-2835.
doi: 10.2514/6.2015-2835

[37] Liu, J., Kailasanath, K., and Gutmark, E. J., "Similarity Spectra Analysis in Highly Heated Supersonic Jets Using Large-Eddy Simulations," *55th AIAA Aerospace Sciences Meeting*, 9-3 January 2017, Grapevine, TX; AIAA 2017-0926.
doi: 10.2514/6.2017-0926

[38] McInerny, S. A., "Characteristics and Predictions of Far-Field Rocket Noise," *Noise Control Engineering Journal* **38**(1), 5-16 (1992).
doi: 10.3397/1.2827802

[39] Baars, W. J., Murray, N. E., and Tinney, C. E., "A proper framework for studying noise from jets with non-compact sources," *Journal of Fluid Mechanics* **929**, A23 (2021).
doi: 10.1017/jfm.2021.837

[40] Swift, S. H., Gee, K. L., Neilsen, T. B., Wall, A. T., Downing, J. M., and James, M. M., "Spatiotemporal Correlation Analysis of Jet Noise from a Round-Nozzle Supersonic Aircraft," *2018 AIAA/CEAS Aeroacoustics Conference*, 25-29 June 2018, Atlanta, GA; AIAA 2018-3938.
doi: 10.2514/6.2018-3938

[41] Olaveson, T., Harker, B. M., and Gee, K. L., "Beamforming-based wavepacket model for noise predictions of tactical aircraft," *Proc. Mtgs. Acoust.* **29**, 040011 (2016).
doi: 10.1121/2.0001639

[42] Papamoschou, D., "Wavepacket Modeling of the Jet Noise Source," *17th AIAA/CEAS Aeroacoustics Conference (32nd AIAA Aeroacoustics Conference)*, 05-08 June 2011, Portland, OR; AIAA 2011-2835.
doi: 10.2514/6.2011-2835

[43] Harker, B. M., Neilsen, T. B., Gee, K. L., Wall, A. T., and James, M. M., "Spatiotemporal Correlation Analysis of Jet Noise from a High-Performance Military Aircraft," *AIAA J.* **54**(5)*,* 1554-1566.
doi: 10.2514/1.J054442

[44] Wall, A. T., Gee, K. L., Neilsen, T. B., Harker, B. M., McInerny, S. A., McKinley, R. L., and James, M. M., "Investigation of multi-lobed fighter jet noise sources using acoustical holography and partial field decomposition methods," *21st AIAA/CEAS Aeroacoustics Conference,* 22-26 June 2015, Dallas, TX; AIAA 2015-2379.
doi: 10.2514/6.2015-2379

[45] Harker, B. M., Gee, K. L., Neilsen, T. B., Wall, A. T., and James, M. M., "Beamforming-Based Wavepacket Model for Noise Environment Predictions of Tactical Aircraft," *23rd AIAA/CEAS Aeroacoustics Conference,* 05-09 June 2017, Denver, CO; AIAA 2017-4048.
doi: 10.2514/6.2017-4048

[46] Schmidt, O. T., Towne, A., Rigas, G., Colonius, T., and Brès, G. A., "Spectral analysis of jet turbulence," *Journal of Fluid Mechanics* **855**, 953-982 (2018).
doi: 10.1017/jfm.2018.675

[47] Nagamatsu, H. T., Sheer, R. E., and Horvay, G., "Supersonic Jet Noise Theory and Experiments," in *Basic Aerodynamic Research*, NASA SP-207 (1969).

[48] Eldred, K. M., "Prediction of Sonic Exposure Histories," *Proceedings of the Symposium on Fatigue of Aircraft Structures*, 11-13 August 1959, Dayton, OH; WADC TR59-507 (DTIC Accession Number AD0227788).

[49] Eldred, K. M., "Acoustic Loads Generated by the Propulsion System," NASA SP-8072 (1971).

[50] Varnier, J., "Experimental Study and Simulation of Rocket Engine Freejet Noise," *AIAA J.* **39**(10), 1851-1859 (2001).
doi: 10.2514/2.1199

[51] Greska, B., Krothapalli, A, Horne, W., and Burnside, N., "A Near-Field Study of High Temperature Supersonic Jets," *14th AIAA/CEAS Aeroacoustics Conference (29th AIAA Aeroacoustics Conference)*, 5-7 May 2008, Vancouver, BC; AIAA 2008-3026.
doi: 10.2514/6.2008-3026

[52] Oertel, H., "Measured Velocity Fluctuations Inside the Mixing Layer of a Supersonic Jet," in *Recent Contributions to Fluid Mechanics*, Springer-Verlag, Berlin, Heidelberg, 1982, pp.170-179.
doi: 10.1007/978-3-642-81932-2_18

[53] Chen, S., Gojon, R., and Mihaescu, M., "Flow and aeroacoustic attributes of highly-heated transitional rectangular supersonic jets," *Aerospace Science and Technology* **114**, 106747 (2001).
doi: 10.1016/j.ast.2021.106747